UDC 621.314.26
DOI: 10.15587/1729-4061.2026.354290

DEVELOPMENT OF IPSO-TVAC FOR ADAPTIVE CONTROL OF GRID-FORMING INVERTERS IN LOW SCR GRIDS WITH HARDWARE CONSTRAINTS

Pham Hong Thanh
PhD Student*
ORCID: https://orcid.org/0009-0001-3463-7099
Le Van Dai
Corresponding author
Doctor of Technical Sciences*
E-mail: levandai@iuh.edu.vn
ORCID: https://orcid.org/0000-0001-9312-0025
*Industrial University of Ho Chi Minh City
Nguyen Van Bao, 12, Hanh Thong Ward,
Ho Chi Minh, Vietnam, 70000

The object of the study is the REGFM-B1-based battery energy storage system (BESS) grid-forming inverter control system operating in weak grids with a short-circuit ratio (SCR) below 2.0. The work focuses on optimizing the virtual synchronous machine (VSM) controller parameters using an improved particle swarm optimization with time-varying acceleration coefficients (IPSO-TVACs). The primary challenge addressed is the failure of conventional tuning methods to converge under three concurrent hardware constraints, including current saturation at 1.2 pu, measurement latency of 10 ms, and ADC quantization noise of 0.01 pu, which form a non-convex search landscape. The proposed IPSO-TVAC is benchmarked against standard PSO (Std-PSO) and gradient-based algorithms, which often converge to physically infeasible solutions under the specified hardware restrictions. The findings reveal that IPSO-TVAC greatly outperforms the standard approaches, with integral of time-weighted absolute error (ITAE) decreased by 16.1%, convergence standard deviation below 1×10^{-4}, and active power ripple lowered from 0.03 pu to below 0.005 pu. These gains suggest that IPSO-TVAC is highly effective in robust transient performance across all investigated constraint combinations. The method's major benefit lies in its fractional-order inertia decay and derivative-penalized cost function, which enable simultaneous management of current-saturation non-convexity and ADC noise sensitivity within a single optimization cycle. The findings imply that IPSO-TVAC is especially advantageous for utility-scale battery storage in distant microgrids, island-grid and offshore wind farms, where consistent frequency stability under inverter overcurrent restrictions and ADC noise during grid transitions is critical

Keywords: grid-forming inverter, REGFM-B1, IPSO-TVAC, Low-SCR weak grids, BESS, hardware constraints

Received 10.02.2026
Received in revised form 16.03.2026
Accepted 15.04.2026
Published 30.04.2026

How to Cite: *Thanh, P. H., Dai, L. V. (2026). Development of IPSO-TVAC for adaptive control of grid-forming inverters in low SCR grids with hardware constraints. Eastern-European Journal of Enterprise Technologies, 2 (5 (140)), 25–35. https://doi.org/10.15587/1729-4061.2026.354290*

1. Introduction

The displacement of synchronous generators by inverter-based resources introduces two coupled challenges: loss of synchronizing torque and reduced short-circuit strength [1]. North American Electric Reliability Corporation (NERC) reliability assessments quantify this risk: when IBR penetration exceeds 50% in regional clusters, systems exhibit insufficient inertia to suppress rate-of-change-of-frequency (RoCoF) below grid code thresholds, typically 1.0 Hz/s [2], during generator outages or transmission faults. Recent updates in IEEE Std 2800–2022 mandate stricter ride-through capabilities for IBRs, necessitating advanced control strategies beyond conventional standards [3].

Virtual synchronous machine (VSM) technology addresses this by encoding the swing equation into inverter control algorithms, enabling power electronic converters to provide synthetic inertia and damping [4]. Classical VSM implementations characteristically face a fundamental physical dilemma: a large inertia constant minimizes the initial frequency drop, yet this kinetic buffer heavily prolongs recovery transients; conversely, a high damping coefficient suppresses oscillations but yields a sluggish response that delays grid stabilization. These factors render fixed-parameter VSM configurations unsuitable for practical weak-grid deployment.

Battery energy storage systems (BESS) configured as grid-forming (GFM) inverters are increasingly deployed in industrial microgrids and islanded grids where centralized generation is unavailable, making frequency stability and hardware protection concurrent critical engineering requirements.

The lack of systematic parameter-tuning methods that account for these physical hardware limitations often leads to control instability or physically unrealizable configurations. Establishing robust optimization frameworks capable of navigating the complex, non-convex control landscapes introduced by hardware saturation and analog-to-digital converter (ADC) noise is essential for the safe and reliable operation of modern power systems. Consequently, developing a systematic optimization framework that explicitly incorporates hardware saturation and measurement noise into the VSM tuning process is critical for grid-code compliance and hardware protection in low-SCR environments [2, 3].

2. Literature review and problem statement

The paper [4] presents results from research on foundational VSM technology, in which synchronverters encode the electromechanical swing dynamics directly into the inverter control loop. This approach demonstrates that it enables synthetic inertia and damping for seamless integration into conventional power systems. Nevertheless, conventional synchronous converter implementations rely on fixed parameters optimized solely for nominal operating points, which degrade transient performance during severe grid disturbances [4]. Such static parameterizations often fail to accommodate severe disturbances, particularly in weak SCR environments characterized by frequent fluctuations in grid impedance. To mitigate these limitations, adaptive control laws, inertia-switching mechanisms, and systematic optimization frameworks have been proposed as viable strategies to enhance transient robustness.

Adaptive extensions of this approach are surveyed in [5]; however, unresolved issues remain related to reliance on simplified system models. While the surveyed strategies propose adaptive inertia variation based on frequency deviations, demonstrating that enhancing inertia during transients can reduce RoCoF and accelerate recovery, the proposed adaptive laws remain limited. A major hurdle in these adaptive designs is the inclusion of hardware current saturation, which introduces non-differentiable constraints. Consequently, their applicability is severely restricted during fault conditions, as current clipping fundamentally alters the achievable control bandwidth.

Similarly, [6] introduces an alternating moment-of-inertia strategy that switches between high and low inertia values to improve damping during load steps. But there were unresolved issues related to noise measurement amplification. Rapid inertia switching increases sensitivity to high-frequency measurement artifacts, including ADC quantization errors, which poses a barrier to implementation on resource-constrained platforms.

In parameter tuning, work in [7] coordinates inertia and damping to improve time-weighted absolute error metrics across various disturbance scenarios. Despite these advancements, parameter selection still relies on manual tuning based on empirical rules. Navigating the non-convex objective landscape created by current saturation boundaries is inherently complex. As a result, gradient-based methods often fail to reach globally optimal solutions without the guidance of a systematic optimization framework.

To address grid variations, [8] demonstrates that online grid impedance estimation enables real-time parameter adaptation under varying grid conditions. However, there is a gap in the absence of a systematic optimization framework for the core VSM parameters. Without noise-regularizing cost functions, the stability margins of these adaptive laws remain highly sensitive to measurement noise, thereby increasing the risk of power oscillations under electromagnetic interference.

Addressing hardware fault protection directly, paper [9] presents a priority current limiting strategy (PCLS) to preserve inner-loop stability during severe faults. Findings reveal that this approach establishes a theoretical basis for angle-preserving current clipping. However, the focus remains on fault ride-through rather than parameter optimization. Applying parameter optimization in this context is problematic, primarily because standard algorithms suffer from convergence degradation due to the discontinuous control response caused by current clipping.

Alternative optimization strategies are examined in [10], where an adaptive VSM controller is tuned using a bang-bang optimization method. The study confirms that meta-heuristic approaches bypass local optima more effectively than gradient-based methods under discontinuous objective landscapes. However, unresolved issues persist related to the introduction of high-frequency discontinuities. Furthermore, such high-frequency switching operations inherently increase the risk of exacerbating chattering in the active power trajectory.

Comprehensive analyses in [11] provide a review of overcurrent-limiting strategies for GFM inverters, classifying them into direct and indirect methods. The study confirms that direct current-reference saturation creates discontinuous gradients in the control landscape, fundamentally altering the achievable dynamic response. Despite this insight, a parameter optimization framework capable of navigating these nonlinearities remains lacking. Standard gradient-based optimization methods fail at non-differentiable points introduced by saturation limiters, necessitating the use of derivative-free metaheuristics. Furthermore, optimization that disregards these physical boundaries consistently yields parameter sets that are mathematically optimal but physically unrealizable in hardware.

Concurrently, data-driven methodologies have emerged. Reference [12] implements a twin delayed deep deterministic policy gradient (TD3) architecture to learn adaptive inertia and damping trajectories directly from closed-loop system feedback. Results demonstrate superior frequency regulation compared to conventional fixed-parameter methods without requiring an analytical system model. The approach requires comparatively high computational effort relies on high-fidelity simulation platforms for generating representative training data, which may constrain its direct applicability in industrial environments with limited offline computational and simulation resources. In particular, the need to retrain the reinforcement learning agent following any structural change in network topology incurs prohibitive computational costs, severely limiting its practicality for resource-constrained industrial applications.

Analysis of research studies [4–12] identifies the need for a unified optimization framework that reconciles high-performance transient response with hardware saturation constraints in low-SCR grids. Ultimately, the non-convex, discontinuous control landscape caused by current limits, coupled with the high sensitivity of adaptive laws to ADC quantization noise, creates a critical need for a unified optimization framework. These three interrelated unresolved challenges, specifically hardware saturation-induced non-convexity, noise sensitivity, and parameter realizability, establish the motivation for developing IPSO-TVAC. The combination of a noise-regularizing cost function and a robust meta-heuristic solver offers a promising approach to achieving globally optimal VSM parameters that are physically realizable and resilient to measurement noise in modern power systems. Such a framework must incorporate a noise-regularizing cost function, operate within physically realizable parameter bounds, and employ a derivative-free solver capable of navigating the non-convex objective landscape.

3. The aim and objectives of the study

The study aims to develop an improved particle swarm optimization with time-varying acceleration coefficients (IPSO-TVAC) for adaptive VSM parameter tuning in GFM inverters under hardware saturation constraints, implemented on the REGFM-B1-based BESS model that incorporates current saturation at 1.2 pu, a 10 ms measurement latency, and ADC quantization noise of 0.01 pu.

To achieve this aim, the following objectives were accomplished:

– to propose a conceptual framework and algorithmic flowchart for improving adaptive VSM parameter tuning under hardware constraints, establishing the structural basis for the IPSO-TVAC optimization engine;

– to evaluate the convergence performance and statistical reliability of IPSO-TVAC against standard PSO (Std-PSO) baselines under hardware-constrained non-convex optimization landscape;

– to analyze the transient dynamic response under severe grid faults and weak-grid conditions using the 15 s multi-stage stress test;

– to verify noise immunity, active power ripple suppression, and large-signal transient stability under weak-grid conditions with SCR below 2.0.

4. Materials and methods

4. 1. The object and hypothesis of the study

The object of the study is the REGFM-B1-based BESS grid-forming inverter control system, selected in accordance with NERC and Western Electricity Coordinating Council (WECC) weak-grid integration guidelines, where the REGFM-B1 configuration is explicitly recommended as a benchmark grid-forming model for assessing inverter-based resource behavior under low system strength conditions. Accordingly, the system is modelled to operate under a short-circuit ratio (SCR) below 2.0, representing severe weak-grid scenarios commonly observed in renewable-dominated power systems.

The system encompasses the entire control chain from the VSM algorithm to the priority current limiting strategy, thereby capturing not only the intended inertial and damping emulation behavior, but also the non-ideal interactions introduced by measurement latency, ADC quantization noise, and current saturation constraints, which are known to critically influence frequency stability and transient performance in digitally implemented GFM inverters.

The principal hypothesis assumes that an optimization framework utilizing the IPSO-TVAC algorithm, applied to minimize a modified integral of time-weighted absolute error (ITAE) cost function that penalizes the active power derivative, will identify a physically realizable parameter set that resolves the conflict between large-signal disturbance rejection and high-frequency noise amplification in adaptive VSM control under hardware current saturation constraints.

Based on the identified limitations of gradient-based and fixed-parameter tuning methods under current-saturated non-convex landscapes, the following testable hypotheses are formulated:

1. Hypothesis 1: global convergence behavior of IPSO TVAC under current saturated non-smooth optimization landscapes and its implications for escaping saturation-induced local optima in grid-forming inverter control. The IPSO-TVAC algorithm is expected to reduce the likelihood of entrapment in local optima induced by the 1.2 pu current saturation boundary by maintaining sufficient swarm momentum during early exploration, thereby achieving superior global ITAE convergence, particularly in regions of the parameter space where saturation-induced non-smoothness degrades the effectiveness of gradient-based search methods.

2. Hypothesis 2: noise-aware constraint induced by the modified ITAE formulation and how this constraint mitigates noise amplification in digitally implemented VSM control loops subject to measurement noise and delay. The modified ITAE cost function is formulated to discourage the selection of excessively high-gain adaptive parameters because such parameter combinations, although capable of reducing short-term frequency error, tend to amplify high-frequency measurement noise through the discrete-time implementation of the control loop, and induce limit-cycle oscillations in digitally implemented VSM controllers, particularly under ADC quantization noise and latency effects.

3. Hypothesis 3: statistical repeatability of IPSO-TVAC under current-saturated non-convex tuning landscapes and why such repeatability is relevant for practical controller parameter commissioning. The IPSO-TVAC algorithm is expected to produce an ITAE standard deviation on the order of 1×10^{-4} across 10 independent optimization runs, indicating a degree of run-to-run consistency which, from an engineering perspective, suggests a level of statistical repeatability compatible with practical controller commissioning procedures.

Assumptions made in the study are: the main grid can be adequately modeled as a Thevenin equivalent circuit to emulate weak-grid dynamics; and the background ADC quantization noise falls consistently within the 0.005–0.01 pu margin.

Simplifications adopted in the study are: The three-phase voltage-source inverter is modeled as an average-value system, intentionally excluding high-frequency switching harmonics to focus computational resources on transient stability and low-frequency control dynamics.

4. 2. REGFM-B1-based grid-forming inverter model

The GFM BESS, based on the REGFM-B1 architecture, recommended by WECC and NERC for GFM resources in weak grids, is adopted [2]. The configuration integrates four physical stages: a DC source representing the BESS, governed by hardware saturation limits; a three-phase voltage-source inverter modeled as an average-value system to capture transients; an LCL filter; and a grid interface consisting of a coupling transformer and a transmission line. The main grid is modeled as a Thevenin equivalent with impedance Z_g to emulate weak-grid conditions, with grid strength characterized by an SCR ranging from 1.5 to 3.0, consistent with weak-grid classifications in IEEE Std 2800-2022 and NERC guidelines for low-inertia systems [2, 3]. Fig. 1 provides the schematic representation of the proposed GFM inverter system and serves to clarify the physical configuration and power flow paths that underpin the subsequent control model.

The control philosophy follows the VSM approach [4]. The virtual rotor dynamics are described by the swing equation in the per-unit system

$$2H(t)\frac{d\omega(t)}{dt} = P_m(t) - P_e(t) - D_p\left(\omega(t) - \omega_n\right), \qquad (1)$$

where $H(t)$ – the virtual inertia constant, $P_m(t)$ – the virtual mechanical input power, $P_e(t)$ – the measured active power, $\omega(t)$ – the virtual angular frequency, and D_p – the damping coefficient. This formulation explicitly links the virtual rotor acceleration to the instantaneous active power imbalance, thereby enabling the virtual inertia term to directly shape transient frequency dynamics under weak-grid conditions where synchronizing torque is inherently limited. The reactive power-voltage loop regulates the internal voltage magnitude $E(t)$.

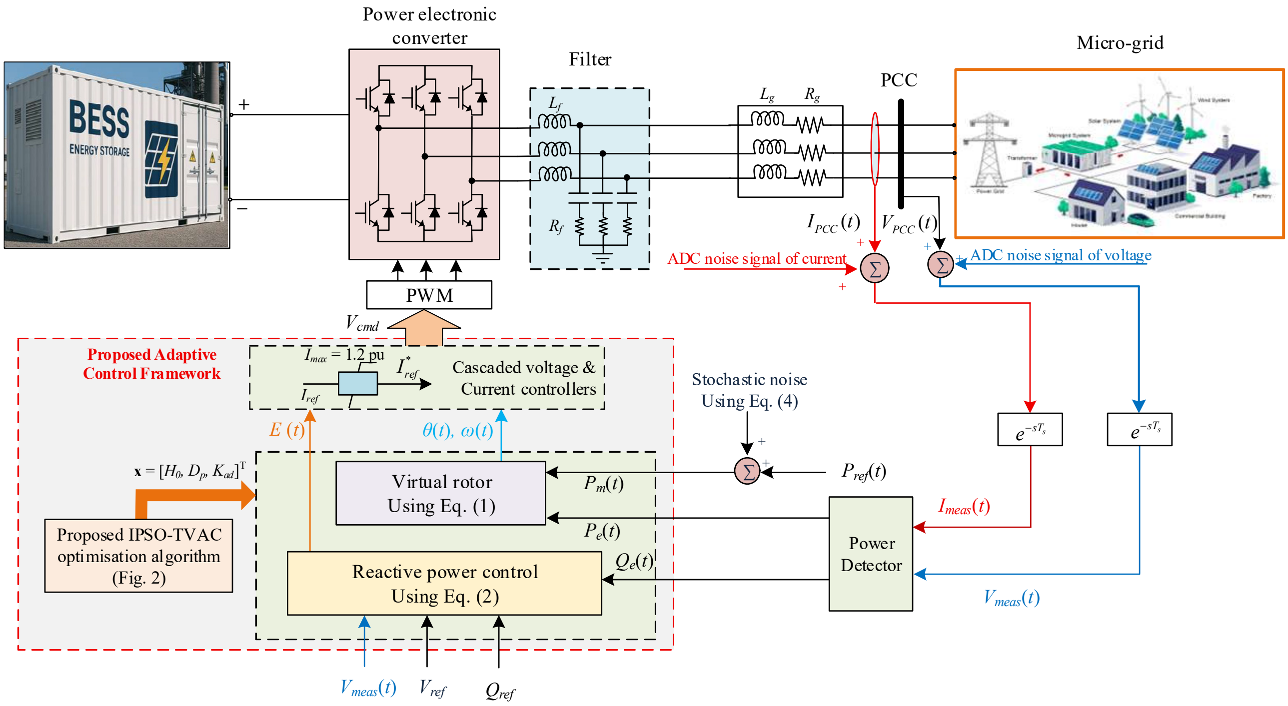

Fig. 1. Schematic diagram of the grid-forming battery energy storage system based on the REGFM-B1 architecture connected to a weak grid

Through this reactive power-voltage coupling, the internal voltage magnitude is dynamically regulated to support voltage stability at the point of common coupling, which becomes particularly critical in low-SCR grids where voltage sensitivity to reactive power variations is pronounced

$$T_v \frac{dE(t)}{dt} = Q_{ref} - Q_e(t) + k_q\left(V_{ref} - V_{meas}(t)\right), \tag{2}$$

where k_q – the reactive droop coefficient, and T_v – the exciter time constant.

4. 3. Adaptive inertia law and priority current limiting strategy

An adaptive inertia law [5, 6] is employed, whereby the effective inertia constant is expressed as a function of the absolute frequency deviation

$$H(t) = H_0 + K_{ad}\left|\omega(t) - \omega_n\right| \le H_{\max}, \tag{3}$$

where $H_{\max}$ – the physical upper limit of the virtual inertia constant, established to prevent dynamic instability during excessively large frequency deviations, the damping coefficient D_p is constant during operation but is optimally tuned offline alongside H_0 and K_{ad}. The law provides stronger inertial support proportional to the severity of the frequency dip. The adaptive law has been shown to enhance transient stability in weak grids [6, 7]. However, the stability margin is sensitive to measurement noise [8].

The PCLS limits the reference current to the 1.2 pu hardware threshold by scaling the direct and quadrature-axis references, thereby preserving the phase angle and maintaining inner-loop stability during faults [9]. However, this nonlinear truncation introduces discontinuities in the objective landscape, potentially leading to premature convergence in standard heuristic algorithms [11, 13, 14].

To reflect practical operations, the DC-source active power $P_m(t)$ includes a dispatch reference and stochastic noise components

$$P_m(t) = P_{ref}(t) + A_{LF}\sin\left(2\pi f_{LF} t\right) + \\ + A_{HF}\sin\left(2\pi f_{HF} t\right), \tag{4}$$

in which, $P_{ref}(t)$ – the active power dispatch reference. The parameters, including A_{LF} and $f_{LF} < 2.0$ Hz define the low-frequency stochastic component simulating wind power fluctuations per the Kaimal spectral density model. The high-frequency components A_{HF} and $f_{HF} > 500$ Hz are physically emulating switching harmonics aliased into the digital control loop due to finite sampling rates [15, 16].

4. 4. Modified integral of time-weighted absolute error cost function formulation

The primary objective of the proposed tuning strategy is to determine the optimal parameter set, including H_0, D_p, and K_{ad} that minimizes frequency deviations while ensuring smooth active power injection and mitigating noise amplification. This objective is formulated under the explicit assumption that the control loop operates in a digitally implemented, current-limited grid-forming inverter, where non-smooth dynamics and measurement artifacts fundamentally alter the achievable transient performance. A modified ITAE cost function is formulated, incorporating penalty terms to limit both control effort and resource utilization because conventional ITAE formulations implicitly assume smooth control trajectories, an assumption that no longer holds once current saturation and discrete time measurement delays are activated in grid forming inverters. The objective function is expressed in Equation (5) as follows, where each term is designed to address a distinct physical limitation arising from current saturation and digital implementation constraints

$$J=\int_0^{T_{sim}} t^{1.5}\cdot\left(w_1\left|\Delta\omega\left(t\right)\right|+w_2\left|\frac{dP_e\left(t\right)}{dt}\right|+w_3H\left(t\right)\right)\mathrm{d}t, \tag{5}$$

where the nonlinear time-weight $t^{1.5}$ focuses optimization on eliminating steady-state errors and prolonged oscillations, thereby prioritizing post-fault settling behavior over short-lived transient excursions, which are already constrained by grid-code frequency limits. The power derivative term $\left|dP_e\left(t\right)/dt\right|$ limits chattering caused by measurement noise and the 10 ms measurement delay. The inertia utilization penalty $w_3H(t)$ prevents excessive mobilization of virtual inertia. The weighting coefficients, including $w_1 = 1.0$, $w_2 = 100$, and $w_3 = 0.01$ were calibrated through a sensitivity-based normalization procedure to ensure commensurate scaling across heterogeneous physical quantities expressed in different units, consisting of Hz, pu, and s. This normalization is necessary to prevent numerical dominance of any single term, which would otherwise bias the optimization toward mathematically convenient but physically unrealistic parameter sets. Specifically, w_2 is amplified to counteract the typically small magnitude of $dP_e\left(t\right)/dt$ relative to frequency deviations, since without such amplification the derivative penalty would become numerically negligible and ineffective in suppressing noise-driven chattering, aligning with established multi-objective control weighting strategies for power electronic converters [10, 16]. The decision vector $\mathbf{x} = [H_0,\ D_p,\ K_{ad}]^{\mathrm{T}}$ is bounded by $H_0 \in [0.5,\ 3.0]$ s, $D_p \in [10,\ 150]$ pu, and $K_{ad} \in [0,\ 300]$ pu, ensuring that all candidate solutions remain physically realizable within the operational limits of grid-forming inverters under current saturation. PSO is employed owing to its simplicity of implementation and rapid convergence in low-dimensional search spaces [17], while remaining inherently derivative-free, which is essential for navigating the non-smooth optimization landscape induced by current saturation and priority current limiting in grid-forming inverters.

4. 5. Implementation procedure and simulation conditions

The proposed optimisation framework is implemented in MATLAB/Simulink, with the REGFM-B1 system constructed per the parameters in Table 1. The algorithm is initialized by randomly distributing 30 particles, bounded by the physical limits $H_0 \in [0.5,\ 3.0]$ s, $D_p \in [10,\ 150]$ pu, and $K_{ad} \in [0,\ 300]$ pu. Full IPSO-TVAC algorithm parameters are provided in Table 1. Each particle configuration is subjected to a comprehensive 15 s multi-stage stress test, with the current saturation limit $I_{\max} = 1.2$ pu actively enforced throughout. The modified ITAE cost index from Equation (5) is computed for each particle; personal best and global best positions are updated; velocity and position updates per equations (6)–(9) are applied. This iterates until the maximum iteration limit is reached. Ten independent runs were executed for each method, and statistical significance was assessed via the Wilcoxon signed-rank test, following the non-parametric validation protocol established in [18]. Computational performance evaluation was conducted on a dedicated workstation equipped with an Intel Core i7 processor and 32 GB of RAM. Wall-clock execution time was measured for each algorithmic component: PSO velocity and position update operations, and full time-domain simulation of the REGFM-B1 model in MATLAB/Simulink with a fixed-step solver at a 50 μs step size. Total offline tuning duration was recorded across ten independent optimisation runs. The reported computational overhead metrics are presented in Section 5. 3.

Table 1

System parameters of the REGFM-B1 BESS configuration

Parameter	Symbol	Value	Unit
Rated power	S_{base}	10	MVA
Rated voltage	V_{base}	22	kV
Nominal frequency	f_n	50	Hz
Filter inductance	L_f	2.5	mH
Line inductance	L_g	5.0	mH
Current limit	I_{max}	1.2	pu
Virtual impedance	Z_{vi}	$0.05 + j0.1$	pu
BESS max discharge	$P_{\max}$	1.2	pu
BESS min charge	$P_{\min}$	–0.5	pu
Population size		30	particles
Max iterations		40	iterations
$w_{\max}$, $w_{\min}$		0.9, 0.4	dimensionless
c_{1i}, c_{1f}		2.5, 0.5	dimensionless
c_{2i}, c_{2f}		0.5, 2.5	dimensionless
Velocity limit		20	% of range

The 15 s multi-stage stress test follows IEEE 1547-2018 [19] recommendations:

– stage 1, the time from 0 s to 2.0 s: Normal operation with stochastic noise per Equation (4);

– stage 2, the time from 2.0 to 2.2 s: Three-phase symmetrical voltage dip to 0.2 pu;

– stage 3, the time from 7.0 s onward: Line trip increases X_g from 0.3 to 0.8 pu, forcing SCR below 1.5;

– stage 4, the time from 12.0 s onward: Load step increases active power reference from 0.9 to 1.1 pu.

5. Results of studying the improved particle swarm optimization for grid-forming inverters control

5. 1. Conceptual framework and algorithmic structure of the proposed improved particle swarm optimization with time-varying acceleration coefficients

Standard PSO updates the velocity and position of each particle according to:

$$v_i^{k+1} = wv_i^k + c_1^k r_1\left(P_{best,i} - x_i^k\right) + c_2^k r_2\left(G_{best} - x_i^k\right), \tag{6}$$

$$x_i^{k+1} = x_i^k + v_i^{k+1}, \tag{7}$$

where w – the inertia weight; c_1^k and c_2^k – the cognitive and social acceleration coefficients, respectively; and $r_1, r_2 \in [0, 1]$ – uniformly distributed random variables. The 1.2 pu current limit introduces discontinuous gradients into the objective landscape, which standard PSO encounters during iteration. The implemented time-varying inertia weighting adopts a fractional-power decay strategy

$$w^k = w_{\min} + \left(w_{\max} - w_{\min}\right)\left(1 - \frac{k}{k_{\max}}\right)^{1.5}, \tag{8}$$

where $k_{\max}$ – the maximum number of iterations configured for the algorithm.

The fractional decay exponent of 1.5 was selected to provide a steeper initial inertia weight reduction than linear decay, thereby accelerating the transition from global exploration to local exploitation while maintaining trajectory smoothness, as validated in comparative metaheuristic studies for non-convex power system optimization [20, 21]. Simultaneously, the acceleration coefficients are dynamically modulated via a linear transition mapping

$$c_1^k = c_{1i} + \left(c_{1f} - c_{1i}\right)\frac{k}{k_{\max}},\ c_2^k = c_{2i} + \left(c_{2f} - c_{2i}\right)\frac{k}{k_{\max}}, \qquad (9)$$

where c_{1i}, c_{1f} and c_{2i}, c_{2f} – the initial and final values of the cognitive and social acceleration coefficients, respectively. Equation (9) governs the TVAC, which shifts algorithmic behavior from global exploration in early iterations with high c_1^k and low c_2^k to local exploitation in later stages with low c_1^k and high c_2^k, as illustrated in Fig. 2.

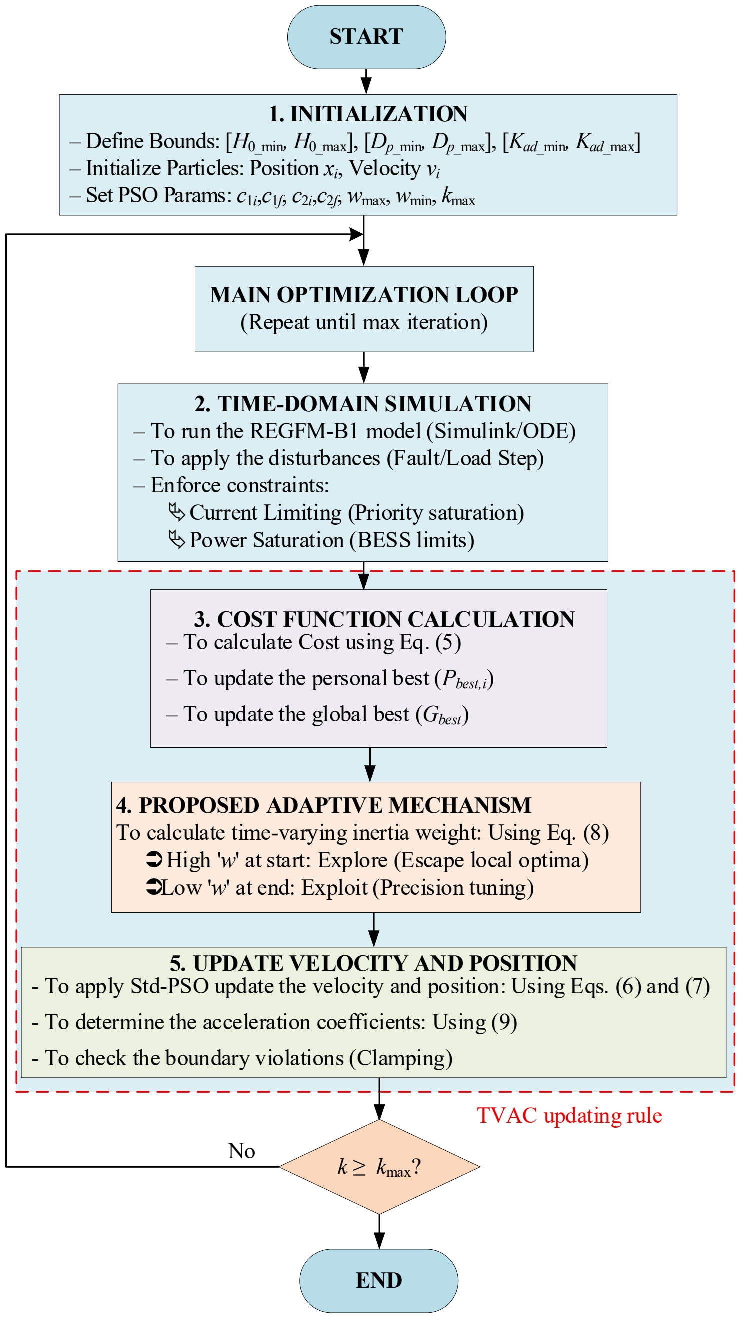

Fig. 2. Flowchart of the improved particle swarm optimization with time-varying acceleration coefficients for virtual synchronous machine parameter tuning

This scheduled transition is essential for navigating the non-convex optimization landscape induced by current saturation, as strong early cognitive influence facilitates boundary crossing and escape from saturation-induced local optima, while increased social influence in later stages promotes convergence consistency and solution stability. The following optimization loop is structured to ensure that all candidate solutions are evaluated under physically enforced current saturation and noise conditions, rather than relying on post-hoc penalty correction, thereby ensuring that infeasible parameter sets are eliminated at the simulation level and that the resulting optimization outcomes remain physically realizable under practical hardware constraints.

The velocity-update mechanism in Equation (6) coordinates with these dynamic parameters: the high initial c_1^k enables particles to explore widely and escape the 1.2 pu current limit trap, while the increasing c_2^k subsequently concentrates the swarm to refine the solution and minimize steady-state oscillations [10, 20]. The fractional-power decay of inertia weight in Equation (8) provides high initial momentum, maintaining elevated step sizes to navigate sharp discontinuous gradients created by the current saturation boundary. Early iteration dynamics steer particles around the fragmented feasible regions imposed by current saturation, reserving fine-grained convergence for later generations [13]. Although differential evolution variants offer superior resistance to premature convergence, their stochastic mutation operations increase per-iteration computational overhead. The proposed PSO algorithm circumvents this bottleneck by using streamlined velocity kinematics as defined in Equations (6) and (7), achieving performance comparable to or better than DE-based approaches at reduced computational cost [21].

The proposed IPSO-TVAC executes five integrated stages iteratively until convergence. However, unlike conventional PSO descriptions that treat these stages as abstract optimization steps, each stage here corresponds to a physically motivated interaction between the controller parameters and the saturated inverter dynamics, ensuring that infeasible solutions are rejected at the simulation level rather than post-processed by penalty functions.

– stage 1, named the initialization: parameter bounds, consisting of H_0, D_p, and K_{ad} are defined. Particle positions, velocities, and control parameters, including c_{1i}, c_{1f}, c_{1i}, c_{1f}, $w_{\min}$, $w_{\max}$, and $k_{\max}$ are initialized within the feasible search space;

– stage 2, named the model execution: a time-domain simulation of the GFM converter model is executed under predefined disturbances, with current limiting and active-power saturation constraints strictly enforced prior to fitness assessment;

– stage 3, named the objective evaluation: the modified ITAE cost function is computed for the current particle set. The personal best of $P_{best,i}$ and global best of G_{best} positions are updated immediately upon identifying a superior objective value;

– stage 4, named the adaptive parameter modulation: the inertia weight w^k is updated via the fractional-power decay strategy. Concurrently, the acceleration coefficients, consisting of c_1^k and c_2^k are modulated to dynamically transition the swarm from global exploration to local exploitation;

– stage 5, named the position and velocity update: positions and velocities are adjusted using standard PSO kinematic equations. Boundary constraints are enforced via position clamping, and the optimization cycle repeats until the maximum iteration threshold is reached.

5. 2. Convergence performance and statistical reliability of the optimization

Table 2 presents the optimised parameter sets, including H_0, D_p, and K_{ad}, and the corresponding ITAE costs averaged across 10 independent runs. The mean ITAE cost for IPSO-TVAC is 24.87 ± 0.00, compared to 29.627 for the fixed-parameter baseline and 24.90 ± 0.02 for Std-PSO. Fig. 3 illustrates the mean convergence trajectories alongside their standard deviation envelopes across 40 iterations.

Table 2

Comparative performance analysis of control methods (mean ± standard deviation)

Methods	ITAE cost	H_0 (s)	D_p (pu)	K_{ad} (pu)
Fixed	29.627 (NA)	3.00 (NA)	100.00 (NA)	0.00 (NA)
Manual	29.41 (NA)	3.00 (NA)	100.00 (NA)	20.00 (NA)
Std-PSO	24.90 ± 0.02	1.11 ± 0.06	47.21 ± 0.68	62.12 ± 12.31
IPSO-TVAC	24.87 ± 0.00	1.16 ± 0.00	47.71 ± 0.08	57.90 ± 0.37

Table 2 reports an ITAE standard deviation of $<1 \times 10^{-4}$ for IPSO-TVAC and 0.02 for Std-PSO. Fig. 3 shows a narrow standard deviation envelope for IPSO-TVAC across all iterations, and a broader spread for Std-PSO during iterations from 35 to 40. Non-parametric validation via the Wilcoxon signed-rank test returns a statistic of $W = 0$ with a p-value < 0.01.

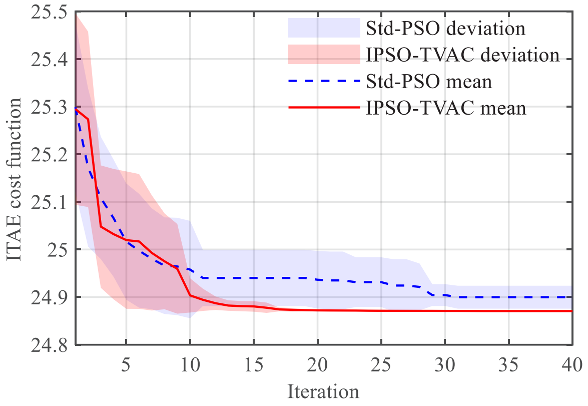

Fig. 3. Optimization convergence trajectories of standard particle swarm optimization and improved particle swarm optimization with time-varying acceleration coefficients over 40 iterations

5. 3. Transient dynamic response under severe grid faults and weak-grid conditions

Fig. 4 presents the time-domain responses of the complete system over the 15 s multi-stage stress test. A zoomed view of the frequency response around the weak-grid transition at 7 s is provided in Fig. 5.

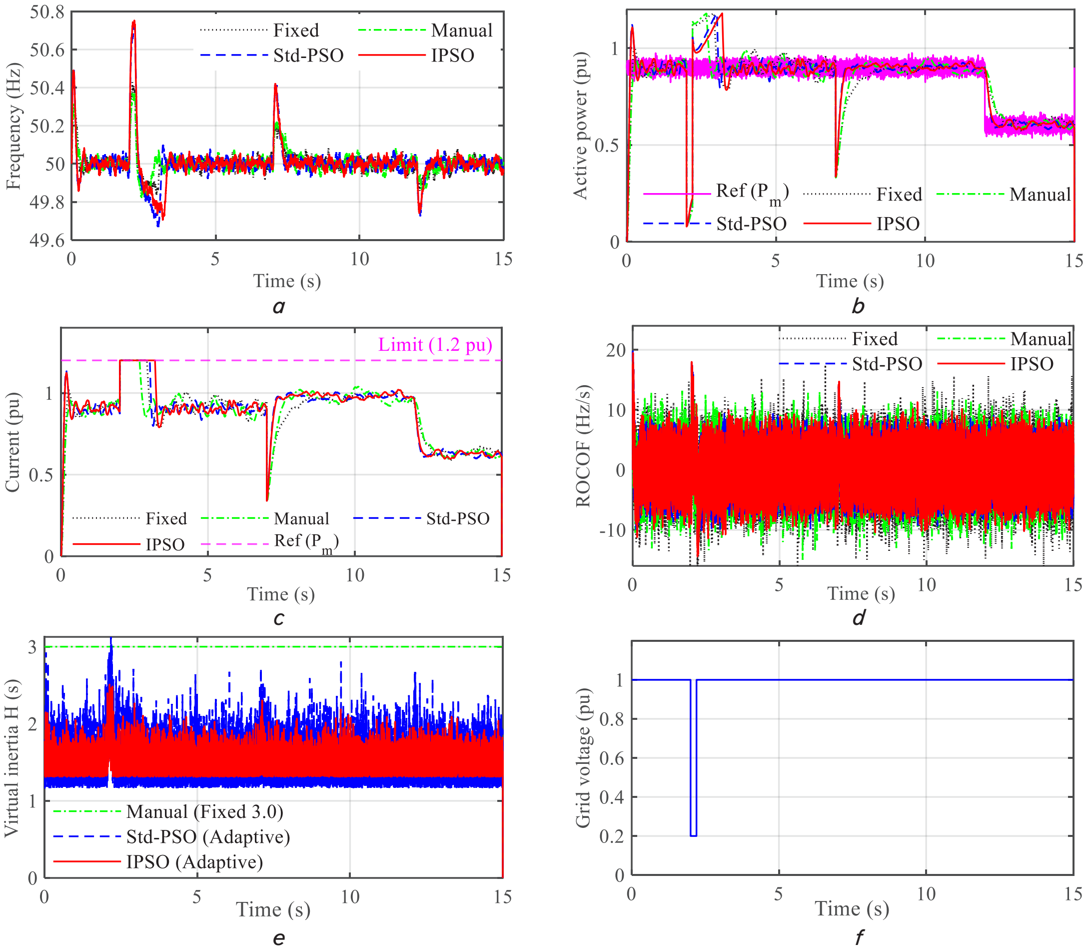

a *b* *c* *d* *e* *f*

Fig. 4. 15 s stress test responses: *a* — frequency; *b* — active power at PCC; *c* — current at PCC; *d* — RoCoF; *e* — adaptive inertia response; *f* — grid voltage profile at PCC

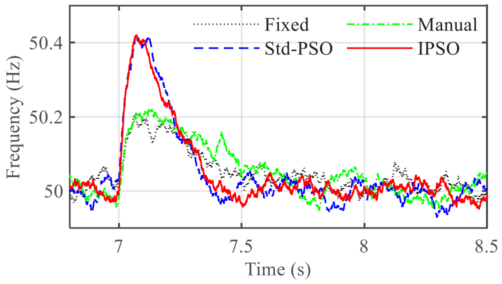

Fig. 5. Zoomed frequency during weak-grid transition at 7 s of Fig. 4, *a*

Fig. 4, *c* shows the inverter output current clamped at $I_{\max} = 1.2$ pu during the 200-ms fault window from 2.0 s to 2.2 s. Fig. 4, *f* shows the corresponding grid voltage dip. Trajectories for system frequency and RoCoF across all disturbance stages are presented in Fig. 4, *a* and Fig. 4, *d*, respectively. At 7 s, the transient frequency peak is 50.43 Hz for IPSO-TVAC and 50.22 Hz for the fixed-parameter baseline, as shown in Fig. 5. The corresponding RoCoF trajectory exhibits a peak magnitude of 20 Hz/s before exponential decay, as shown in Fig. 4, *d*. Active power trajectories for all four control configurations across the disturbance sequence are plotted in Fig. 4, *b*.

5. 4. Noise immunity, active power ripple suppression, and large-signal transient stability

Table 3 quantifies active power ripple magnitude and adaptive inertia stability for both optimization methods at the 12 s load step. Fig. 6 provides a zoomed view of the active power response during this transient event.

Table 3

Quantitative comparison of noise immunity performance at 12 s load step

Metric	Std-PSO	IPSO-TVAC
Peak-to-peak active power ripple (pu)	0.03	< 0.005
Inertia constant variance	high (erratic)	low (stable)
Identified gain K_{ad} (pu)	62.12	57.90
Computation time per iteration (ms)	120	125
Time-domain simulation per run (min)	~ 4.5	~ 4.8
Total offline tuning time (minutes)	~ 45	~ 48

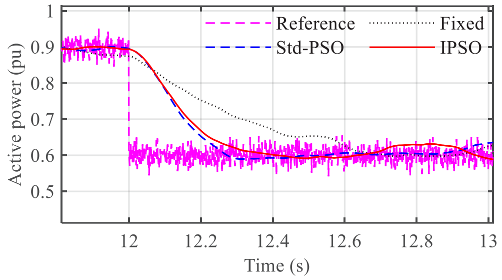

Fig. 6. Zoomed active power at 12 s of Fig. 4, *b*

Table 3 reports a peak-to-peak active power ripple of 0.03 pu for Std-PSO and below 0.005 pu for IPSO-TVAC. The tuned K_{ad} value is 57.90 pu for IPSO-TVAC and 62.12 pu for Std-PSO. Fig. 6 visualizes the chattering amplitude in the active power response induced by 0.005 to 0.01 pu ADC quantization noise during the load step. Fig. 4, *e* shows the adaptive inertia trajectory of $H(t)$ bounded for the full test duration under IPSO-TVAC, and erratic fluctuations under Std-PSO.

Fig. 7 presents the phase-plane portrait mapping frequency deviation of $\Delta\omega$ against rotor angle deviation of $\Delta\delta$ across the full 15 s sequence, with equilibrium points from 1 to 3 aligned to the SCR regimes defined in Section 4. 5.

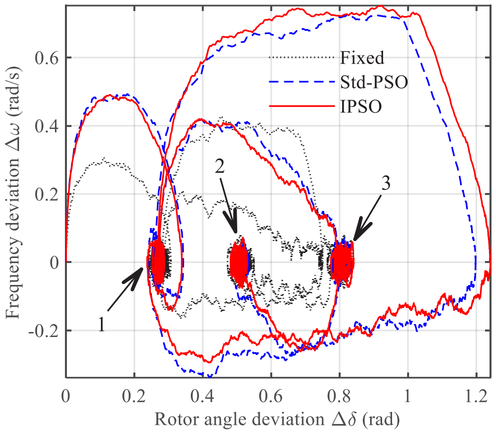

Fig. 7. Phase portrait of $\Delta\omega$ versus $\Delta\delta$ illustrating the evolution of equilibrium points throughout the entire 15 s multi-stage stress test

As shown in Fig. 7, IPSO-TVAC yields monotonically converging trajectories to all three equilibrium points. The phase trajectory remains confined within a bounded region throughout the SCR transitions, including the regime where SCR falls below 1.5 after 7 s.

6. Discussion of improved particle swarm optimization results for grid-forming inverters

The structural features of the proposed IPSO-TVAC algorithm are designed to promote a systematic shift from global exploration to local exploitation. By coupling fractional-power inertia decay with TVAC, the algorithm maintains sufficient initial swarm momentum to traverse the 1.2 pu PCLS discontinuity before concentrating on precision tuning. This architectural design is associated with a reduced tendency toward premature convergence at saturation boundaries, a well-documented limitation in gradient-dependent or fixed-parameter schemes. Subsequent analysis quantifies the operational impact of these framework features on system performance and statistical reliability.

The 16.1% ITAE reduction reported in Table 2 can be interpreted as arising from two interacting mechanisms within the proposed framework, based on the comparative parameter trends and dynamic response metrics reported in Section 5. First, the derivative penalty term $w_2\left|dP_e(t)/dt\right|$ in Equation (5) regularizes the cost function against high-frequency measurement artifacts by increasing sensitivity to rapid active-power variations rather than steady-state deviations. By penalizing rapid power fluctuations, this term steers the optimizer away from high-gain K_{ad} configurations that would otherwise amplify ADC quantization noise of 0.005–0.01 pu into the control loop [16, 22]. Table 2 quantifies the resulting reduction in K_{ad} from 62.12 pu for Std-PSO to 57.90 pu for IPSO-TVAC, which corresponds to an 83% reduction of peak-to-peak active power ripple from 0.03 pu to under 0.005 pu, as reported in Table 3 and visualized in Fig. 6. This suppression of high-frequency current chattering reduces electrochemical stress on energy storage cells, aligning with degradation pathways associated with sustained current ripple [23]. Second, the fractional-power inertia decay strategy in Equation (8) enhances swarm exploration capability. The exponent 1.5, determined via a parametric sensitivity analysis that balances convergence speed and solution stability, represents an empirically selected trade-off rather than a theoretically optimal value, providing sufficient initial momentum for particles to traverse the discontinuous gradient induced by the 1.2 pu PCLS boundary [9, 11]. Under the proposed trajectory control scheme, the inter-run ITAE standard deviation observed for IPSO-TVAC remains $< 1 \times 10^{-4}$, whereas a value of 0.02 is obtained for the standard PSO, as summarized in Table 2. Statistical validation using the Wilcoxon signed-rank test yields $W = 0$ and p-value < 0.01, confirming the stochastic dominance of IPSO-TVAC over Std-PSO at $\alpha = 0.001$ [18].

Operationally, the transient frequency peak of 50.43 Hz for IPSO-TVAC versus 50.22 Hz for the fixed-parameter baseline, as shown in Fig. 5, corresponds to the optimized inertia constant $H_0 = 1.16$ s. This behavior is consistent with the established VSM trade-off: reduced virtual inertia accelerates frequency recovery while permitting a larger initial deviation [4, 7]. The 0.21-Hz difference remains within the ±0.5-Hz operational band specified in IEEE Std 2800-2022 [3], indicating grid-code compliance during weak-grid transitions. The RoCoF spike at 20 Hz/s observed in Fig. 4, *d* results from the accelerated virtual rotor dynamics enabled by the reduced inertia constant. This transient acceleration occurs before the damping torque fully develops during the initial fault window. From a protection coordination standpoint, this RoCoF magnitude falls within the 40–500 ms relay immunity window documented in IEEE Std 2800-2022 and subsequent studies [3, 24, 25], indicating compliance with relay immunity requirements under the tested conditions during the fault transient. The exponential decay of the RoCoF trajectory, as visualized in Fig. 4, *d*, demonstrates that the system returns to permissible bounds before protective relays would initiate disconnection. The phase-plane portrait in Fig. 7 exhibits smooth, monotonic convergence toward all three equilibrium points. This trajectory behavior indicates the presence of positive damping torque across all SCR regimes, including the challenging condition where SCR falls below 1.5 after 7 s [26]. The non-convexity of the objective landscape, arising from the combined effects of stochastic noise excitation defined in equation (4) and PCLS activation at the 1.2 pu current limit, provides a plausible explanation for the observed failure of standard gradient-based tuning to locate globally optimal solutions [11]. The 0.02 ITAE standard deviation reported for Std-PSO in Table 2 is consistent with this structural limitation: within the saturated region, gradients lack consistent directional information, causing premature convergence to sub-optimal, physically infeasible solutions. The present results address the three interrelated challenges identified in Section 2 as follows.

Current-reference saturation fundamentally distorts the optimization landscape by generating non-differentiable gradient discontinuities, a structural characteristic that can induce premature convergence in conventional tuning algorithms [9, 11]. IPSO-TVAC addresses this challenge, achieving near-zero run-to-run ITAE standard deviation $<1 \times 10^{-4}$ across 10 independent runs, compared to 0.02 for Std-PSO, as shown in Table 2 and Fig. 3. The fractional-power inertia decay in Equation (8) provides sufficient swarm momentum to traverse the 1.2 pu PCLS discontinuity, preventing stagnation at the saturation boundary.

The inherent sensitivity of adaptive inertia control laws to measurement noise frequently amplifies low-level ADC quantization errors into sustained active power limit cycles [6, 8]. As quantified in Table 3 and visualized in Fig. 6, IPSO-TVAC suppresses these oscillations, reducing the peak-to-peak active power ripple from 0.03 pu to below 0.005 pu. The derivative penalty $w_2\left|dP_e\left(t\right)/dt\right|$ defined in Equation (5) contributes to noise robustness by penalizing rapid power fluctuations independent of their ITAE contribution, thereby steering the optimizer away from high-gain configurations that amplify measurement artifacts.

Optimization procedures that lack explicit physical boundary enforcement often yield parameter sets that are mathematically optimal but physically unrealizable in practical hardware implementations [11]. IPSO-TVAC addresses this by constraining the search space to physically realizable bounds from initialization. The resulting parameters, consisting of $H_0 = 1.16$ s, $D_p = 47.71$ pu, and $K_{ad} = 57.90$ pu, remain operable throughout the full 15 s stress test, including the 0.2 pu voltage dip and SCR transition below 1.5. Fig. 4, *c* shows that the system operates without any current limit violations beyond the enforced 1.2 pu threshold.

Unlike the alternating-inertia strategy in [6], which exhibits heightened sensitivity to high-frequency ADC quantization errors due to rapid switching, the proposed framework enhances noise robustness while preserving transient performance under the investigated operating conditions. As quantified in Table 3 and visualized in Fig. 6, the peak-to-peak active power ripple is suppressed from 0.03 pu to below 0.005 pu. This improvement is attributed to the derivative penalty term $w_2\left|dP_e\left(t\right)/dt\right|$ defined in Equation (5), which penalizes parameter configurations that amplify measurement noise independently of their ITAE contribution even when such configurations would otherwise yield comparable ITAE values. Consequently, the search is steered away from high-gain K_{ad} configurations that the alternating-inertia approach cannot inherently mitigate.

Relative to the empirical manual tuning approach in [7], which struggles to navigate non-convex saturation landscapes, the present framework achieves ITAE standard deviation $<1 \times 10^{-4}$ across 10 independent runs versus 0.02 for Std-PSO as reported in Table 2 and eliminates sawtooth limit-cycle patterns in the phase portrait of Fig. 7, leveraging the swarm momentum mechanism discussed above.

The TD3 reinforcement learning agent in [12] requires computationally intensive retraining following network topology changes. The parameter set identified by IPSO-TVAC maintains operational robustness across all three SCR regimes during the stress test, including sustained operation under the 1.2 pu hardware limit throughout the 200-ms fault window, as shown in Fig. 4, *c*. Parameter-space bounding restricts the search to a physically feasible region from initialization, ensuring that all candidate solutions inherently comply with hardware constraints. The proposed framework eliminates post-hoc constraint enforcement and agent retraining, whereas reinforcement learning approaches rely on penalty terms that permit constraint violations during training phases. From a commissioning perspective, offline tuning is executed a single time during system deployment. IPSO-TVAC incurs a per-iteration computational overhead of 125 ms compared to 120 ms for Std-PSO, corresponding to a 4.2% increase. This marginal overhead is justified by the 16.1% ITAE improvement and the enhanced statistical reliability demonstrated across independent optimization runs.

The validity of the presented results is subject to three applicability conditions. First, the identified parameter set is validated for the tested SCR range corresponding to grid reactance values of 0.3 to 0.8 pu. Second, the reported noise-immunity margin is valid within the simulated ADC quantization range of 0.005 to 0.01 pu. Third, the average-value inverter model excludes switching-frequency harmonics; consequently, experimental deployment may require minor parameter adjustment to compensate for high-frequency switching dynamics. To ensure simulation reproducibility, implementation requires a fixed-step solver with a step size $\leq 50\,\mu$s and consistent stochastic noise seeds across independent runs.

The current implementation exhibits two limitations worthy of acknowledgment. First, the 48-minute offline commissioning time precludes real-time re-tuning following abrupt topology changes. Consequently, deployments in networks subject to frequent switching events would require pre-computed parameter lookup tables indexed by SCR, adding engineering overhead that partially offsets the commissioning advantage. Second, the fractional exponent 1.5 in Equation (8) was selected empirically based on convergence-smoothness trade-off analysis in preliminary trials. The absence of an analytical derivation for this exponent limits direct cross-platform transferability, as hardware featuring asymmetric saturation limits or current thresholds other than 1.2 pu requires empirical recalibration, given that a standardized tuning framework remains undefined.

Future work could address this by implementing an adaptive exponent law that adjusts the constraint activation rate or by developing a meta-optimization layer to select the exponent based on hardware-specific constraint profiles. A parallel research direction involves a data-driven surrogate model that maps real-time SCR and frequency measurements to the optimal parameter set at millisecond latency, potentially bypassing the 48-minute offline tuning constraint. Key mathematical challenges in this direction include constructing non-convex surrogate models that preserve the physical constraints and discontinuous gradients of the original objective landscape. Extension to multi-inverter weak grids [1, 2] introduces the challenge of coordinated PCLS saturation management across units, where the joint parameter space scales combinatorically with system dimensionality. Quantifying the impedance-based stability margin using the criterion in [27] remains a priority for future analytical work. Finally, hardware-in-the-loop validation on a physical BESS bench with an impedance-scaled grid emulator is required to quantify the impact of switching-frequency harmonics, which are excluded from the average-value model, on the effective PCLS activation threshold. Such harmonics could shift the non-convex boundary and potentially render the identified parameter set suboptimal on the physical platform, necessitating minor parameter fine-tuning.

7. Conclusions

The REGFM-B1-based GFM BESS model, incorporating 1.2 pu priority current limiting, 10-ms measurement latency, and 0.01 pu ADC quantization noise, captures a non-convex optimization landscape that is representative of low-SCR GFM inverter deployments. The modified ITAE cost function integrates the considered hardware limitations into a single scalar objective function suitable for derivative-free optimization:

1. The proposed conceptual framework and algorithmic flowchart define a systematic tuning methodology for adaptive VSM parameters. By integrating fractional-power inertia decay with time-varying acceleration coefficients, the algorithm is designed to promote a gradual transition from global exploration to local exploitation, which is associated with improved navigation of discontinuous constraint surfaces and a reduced tendency toward premature convergence.

2. The IPSO-TVAC algorithm achieves superior statistical reliability under hardware-constrained landscapes, converging to a physically realizable parameter set including $H_0 = 1.16$ s, $D_p = 47.71$ pu, and $K_{ad} = 57.90$ pu. Across 10 independent runs, the framework observed ITAE standard deviation remains below 1×10^{-4}, compared to 0.02 for Std-PSO. The fractional-power inertia decay is associated with more consistent global convergence behavior without premature stagnation at the 1.2 pu saturation boundary.

3. Time-domain analysis under the 15 s multi-stage stress test indicates stable transient dynamic behavior. IPSO-TVAC reduces the ITAE index by 16.1% relative to the fixed-parameter baseline and maintains compliance with the 1.2 pu current limit throughout fault and weak-grid transitions. The optimized configuration yields a transient frequency peak of 50.43 Hz within the ± 0.5 Hz operational band, RoCoF event duration falling within the 40–500 ms relay immunity window.

4. Noise immunity and large-signal stability are verified under SCR conditions below 2.0. The derivative-penalized cost function eliminates noise-induced limit cycles, reducing peak-to-peak active power ripple from 0.03 pu to below 0.005 pu during load transients. The resulting parameter set maintains bounded adaptive inertia trajectories and stable phase-plane convergence, suggesting suitability for utility-scale BESS applications under the considered conditions without requiring post-optimization hardware redesign or agent retraining.

Conflict of interest

The authors declare that they have no conflict of interest in relation to this study, whether financial, personal, authorship, or otherwise, that could affect the study and its results presented in this paper.

Financing

The study was performed without financial support.

Data availability

Manuscript has no associated data.

Use of artificial intelligence

The authors declare that generative artificial intelligence AI tools were used exclusively for language editing, grammar checking, and technical formatting of the manuscript under full human supervision. The AI tools were not used for the development of scientific content, data analysis, or interpretation of results. All intellectual contributions are solely those of the authors.

Authors' contributions

Pham Hong Thanh: Conceptualization, Methodology, Investigation, Software, Formal analysis, Writing – Original Draft; **Le Van Dai**: Conceptualization, Methodology, Investigation, Software, Formal analysis, Validation, Supervision, Writing – Review and Editing

References

1. Lin, Y., Eto, J. H., Johnson, B. B., Flicker, J. D., Lasseter, R. H., Pico, H. N. V. et al. (2020). Research roadmap on grid-forming inverters. National Renewable Energy Lab. Available at: https://www.nrel.gov/docs/fy21osti/73476.pdf
2. Integrating inverter-based resources into low short circuit strength systems (2017). North American Electric Reliability Corporation (NERC) Atlanta, GA, USA.
3. 2800-2022 - IEEE Standard for Interconnection and Interoperability of Inverter-Based Resources (IBRs) Interconnecting with Associated Transmission Electric Power Systems. https://doi.org/10.1109/ieeestd.2022.9762253
4. Zhong, Q.-C., Weiss, G. (2011). Synchronverters: Inverters That Mimic Synchronous Generators. IEEE Transactions on Industrial Electronics, 58 (4), 1259–1267. https://doi.org/10.1109/tie.2010.2048839
5. Bevrani, H., Ise, T., Miura, Y. (2014). Virtual synchronous generators: A survey and new perspectives. International Journal of Electrical Power & Energy Systems, 54, 244–254. https://doi.org/10.1016/j.ijepes.2013.07.009
6. Alipoor, J., Miura, Y., Ise, T. (2015). Power System Stabilization Using Virtual Synchronous Generator With Alternating Moment of Inertia. IEEE Journal of Emerging and Selected Topics in Power Electronics, 3 (2), 451–458. https://doi.org/10.1109/jestpe.2014.2362530
7. Tang, W., Li, B., Shao, X., Ye, Y., Yu, Y., Chen, J. (2025). An Adaptive Inertia and Damping Control Strategy for Virtual Synchronous Generators to Enhance Transient Performance. Energies, 19 (1), 204. https://doi.org/10.3390/en19010204
8. Roveri, A., Mallemaci, V., Mandrile, F., Bojoi, R. (2025). Enhanced Virtual Synchronous Machine With Online Grid Impedance Estimation. IEEE Open Journal of Industry Applications, 6, 427–444. https://doi.org/10.1109/ojia.2025.3584050
9. Baeckeland, N., Yang, B., Seo, G.-S. (2025). Transient Stability-Enhancing Method for Grid-Forming Inverters Under Current Limiting. IEEE Transactions on Power Electronics, 40 (5), 6714–6725. https://doi.org/10.1109/tpel.2025.3532490
10. Elwakil, M. M., Zoghaby, H. M. E., Sharaf, S. M., Mosa, M. A. (2023). Adaptive virtual synchronous generator control using optimized bang-bang for Islanded microgrid stability improvement. Protection and Control of Modern Power Systems, 8 (1). https://doi.org/10.1186/s41601-023-00333-7
11. Baeckeland, N., Chatterjee, D., Lu, M., Johnson, B., Seo, G.-S. (2024). Overcurrent Limiting in Grid-Forming Inverters: A Comprehensive Review and Discussion. IEEE Transactions on Power Electronics, 39 (11), 14493–14517. https://doi.org/10.1109/tpel.2024.3430316
12. Oboreh-Snapps, O., She, B., Fahad, S., Chen, H., Kimball, J., Li, F. et al. (2024). Virtual Synchronous Generator Control Using Twin Delayed Deep Deterministic Policy Gradient Method. IEEE Transactions on Energy Conversion, 39 (1), 214–228. https://doi.org/10.1109/tec.2023.3309955
13. Kweon, J., Jing, H., Li, Y., Monga, V. (2024). Small-signal stability enhancement of islanded microgrids via domain-enriched optimization. Applied Energy, 353, 122172. https://doi.org/10.1016/j.apenergy.2023.122172
14. Li, X., Clerc, M. (2018). Swarm Intelligence. Handbook of Metaheuristics, 353–384. https://doi.org/10.1007/978-3-319-91086-4_11
15. IEC 61400-1: Wind turbines – Part 1: Design requirements (2005). International Electrotechnical Commission. Available at: https://cdn.standards.iteh.ai/samples/12556/5a25eb41347f46b9b293e5f30c8eb7a4/IEC-61400-1-2005.pdf
16. Buso, S., Mattavelli, P. (2006). Digital Control in Power Electronics. Springer International Publishing. https://doi.org/10.1007/978-3-031-02495-5
17. Nassef, A. M., Abdelkareem, M. A., Maghrabie, H. M., Baroutaji, A. (2023). Review of Metaheuristic Optimization Algorithms for Power Systems Problems. Sustainability, 15 (12), 9434. https://doi.org/10.3390/su15129434
18. Rivas-Martínez, G. I., Rodas, J., Herrera, E., Doval-Gandoy, J. (2025). A Novel Approach to Performance Evaluation of Current Controllers in Power Converters and Electric Drives Using Non-Parametric Analysis. IEEE Latin America Transactions, 23 (1), 68–77. https://doi.org/10.1109/tla.2025.10810402
19. 1547-2018 – IEEE Standard for Interconnection and Interoperability of Distributed Energy Resources with Associated Electric Power Systems Interfaces. https://doi.org/10.1109/ieeestd.2018.8332112
20. Ratnaweera, A., Halgamuge, S. K., Watson, H. C. (2004). Self-Organizing Hierarchical Particle Swarm Optimizer With Time-Varying Acceleration Coefficients. IEEE Transactions on Evolutionary Computation, 8 (3), 240–255. https://doi.org/10.1109/tevc.2004.826071
21. Syed, D., Shaikh, G. M., Alshahrani, H. M., Hamdi, M., Alsulami, M., Shaikh, A., Rizwan, S. (2024). A Comparative Analysis of Metaheuristic Techniques for High Availability Systems. IEEE Access, 12, 7382–7398. https://doi.org/10.1109/access.2024.3352078
22. Teodorescu, R., Liserre, M., Rodríguez, P. (2010). Grid Converters for Photovoltaic and Wind Power Systems. John Wiley & Sons. https://doi.org/10.1002/9780470667057
23. Muñoz-Torrero, D., García-Quismondo, E., Ventosa, E., Prodanovic, M., Palma, J. (2025). On the degradation of lithium-ion batteries over a current ripple effect. Electrochimica Acta, 530, 146326. https://doi.org/10.1016/j.electacta.2025.146326
24. Milano, F., Dörfler, F., Hug, G., Hill, D. J., Verbič, G. (2018). Foundations and Challenges of Low-Inertia Systems (Invited Paper). 2018 Power Systems Computation Conference (PSCC), 1–25. https://doi.org/10.23919/pscc.2018.8450880
25. Xu, X., Yousefian, R., Elkhatib, M., Choi, B., Huang, L., Mao, Y., Berner, A. (2019). Automatic Underfrequency Load Shedding Study of the PJM System. 2019 IEEE Power & Energy Society General Meeting (PESGM), 1–5. https://doi.org/10.1109/pesgm40551.2019.8973420
26. Grigsby, L. L. (Ed.) (2017). Power System Stability and Control. CRC Press. https://doi.org/10.4324/b12113
27. Ohuchi, K., Masod, A. F. B., Kato, S., Hirase, Y. (2023). Stability analysis of virtual synchronous generator control in a high-voltage DC transmission system using impedance-based method. Energy Reports, 9, 557–567. https://doi.org/10.1016/j.egyr.2022.11.077